Journal of Power Sources 302 (2016) 70–78

Contents lists available at ScienceDirect

Journal of Power Sources

journal homepage: www.elsevier.com/locate/jpowsour

Porous spherical polyacrylonitrile-carbon nanocomposite with high loading of sulfur for lithium–sulfur batteries

Hiesang Sohn [a], Mikhail L. Gordin [a], Michael Regula [b], Dong Hyeon Kim [c], Yoon Seok Jung [c], Jiangxuan Song [a], Donghai Wang [a, *]

[a] The Pennsylvania State University, Department of Mechanical and Nuclear Engineering, University Park, PA 16802, USA
[b] The Pennsylvania State University, Department of Chemical Engineering, University Park, PA 16802, USA
[c] Ulsan National Institute of Science and Technology (UNIST), School of Energy and Chemical Engineering, Ulsan 689-798, Republic of Korea

HIGHLIGHTS

- Porous nanocomposite of sulfur/pyrolyzed polyacrylonitrile-Ketjenblack(*p*PAN-KB/S).
- Preparation of *p*PAN-KB/S (*ca.* 72%) by an aerosol process as Li–S battery cathode.
- Combined abilities of KB(high conductivity, physisorption) & *p*PAN(chemisorption).
- Superior performance of *p*PAN-KB/S to *p*PAN/S and KB/S with similar sulfur loading.
- *p*PAN-KB/S with high sulfur loading (*ca.* 4.4 mg-S/cm^2) exhibits good performance.

ARTICLE INFO

Article history:
Received 6 August 2015
Received in revised form
3 October 2015
Accepted 7 October 2015
Available online 24 October 2015

Keywords:
Li-S batteries
Aerosol process
Conductivity
Porosity
Chemical functionality

ABSTRACT

Pyrolyzed porous spherical composites of polyacrylonitrile-Ketjenblack carbon and sulfur (*p*PAN-KB/S) with a high sulfur content (*ca.* 72%) and enhanced conductivity and porosity (pore volume: 1.42 cm^3/g; BET surface area: 727 m^2/g) were prepared by an aerosol-assisted process and applied as cathode for lithium-sulfur batteries. Electrochemical tests showed that the *p*PAN-KB/S composite exhibited a high capacity of 866 mAh/g (based on sulfur) after 100 cycles at 0.5C (1C = 1.68 A/g) and a good rate performance at high current density (431 mAh/g at 5C). In addition, a *p*PAN-KB/S composite electrode with high sulfur loading (*ca.* 4.4 mg-S/cm^2) exhibited impressive electrochemical performance with a reversible capacity of 513 mAh/g and 576 mAh/cm^3 (based on sulfur) and a coulombic efficiency >99% after 100 cycles at 0.5C.

1. Introduction

Due to the increasing demand for renewable energy storage systems with high energy and power density, there has recently been keen interest in exploring new high-capacity electrode materials for rechargeable lithium-ion batteries [1,2]. However, the capacity of conventional cathode materials, such as lithium transition metal oxides and phosphates, is inherently limited to less than 300 mAh/g [1,2]. In contrast, elemental sulfur (S_8) has a high theoretical specific capacity (1672 mAh/g) and energy density (2600 Wh/kg) while being low-cost, naturally abundant, and environmentally benign [2–4]. Because of these characteristics, sulfur has received significant attention as a cathode material for next-generation energy storage, but several key issues have thus far hindered practical application of lithium-sulfur (Li–S) batteries. These issues include the inherently low conductivity of sulfur and the lithium polysulfide shuttle phenomenon [1–5]. The low electrical conductivity of sulfur (5×10^{-30} S/cm at 25 °C) necessitates the use of a large amount of electrochemically-inactive conductive carbon to improve utilization of the active material [2–5]. In addition, the polysulfide shuttling phenomenon at the initial lithiation stage of each cycle leads to a loss of active material by irreversible deposition of lithium sulfide (Li_2S, Li_2S_2) on both electrodes and, thus, poor efficiency [2–5]. To address these problems, considerable efforts have been devoted to sulfur-based cathode

* Corresponding author.
E-mail address: dwang@psu.edu (D. Wang).

http://dx.doi.org/10.1016/j.jpowsour.2015.10.013
0378-7753/

materials that either encapsulate sulfur into porous conductive media or utilize chemical bonding or chemisorption to keep sulfur and polysulfides electrochemically active [2–4,6].

Porous conductive media such as carbon nanotubes [7], porous carbon fibers [8], graphene [9], carbon paper interlayers [10], meso- and microporous carbons [2,4,11–14], and conducting polymers [15] have been shown to enhance the conductivity of sulfur-based cathodes as well as to encapsulate sulfur and thus prevent dissolution of polysulfides [2,4,5,11–15] by weak physical adsorption of sulfur and lithium polysulfides/sulfide on carbon [2,4,5,11,12,14,16]. Particularly, the works based on porous carbon-sulfur composite showed that the capacity is dependent on the BET surface area, pore structure and porosity of the carbon by comparing the electrochemical performance of carbon-sulfur composites [11–14]. Jeong et al. and Liang et al. showed that the capacity is dependent on the BET surface area of the carbon [11]. In addition, Jozwiuk et al. compared the performance of carbon blacks with different BET surface areas and additionally showed the difference in polysulfide adsorption ability [11]. Strubel et al. and Schuster et al. demonstrated that the electrochemical performance of Li–S battery can be largely dependent on the porosity and specific surface area of host carbon [12]. On the other hand, by regulating pore structure of the carbon, Zhang et al. demonstrated high performance Li–S battery based on microporous carbon/sulfur composite with less than 50% sulfur loading [13]. Recently, Sohn et al. showed the rate capability can be largely dependent on the porosity and pore size of porous carbon [14].

Solely dependent on physisorption of sulfur and polysulfides, these materials still suffer from low active material utilization. Rather than relying on weak physical absorption, the application of functional media with the ability to chemisorb polysulfides, such as pyrolyzed Polyacrylonitrile [17–25], metal oxides [26], graphene oxides [27], and doped carbons [6,28,29] have recently been reported to enhance sulfur utilization and enable a uniform distribution of sulfur and lithium sulfide in the cathode material [2,6,28,29]. Zhang et al. used graphene oxide as a sorption framework for sulfur, taking advantage of the chemical interaction between sulfur and functional groups on graphene oxide to efficiently improve the utilization of active materials and reduce the shuttle effect [27]. Guo et al. demonstrated a Li_2S-carbon composite cathode with a high charge/discharge capacity and a good coulombic efficiency, demonstrating the ability of the lithium–nitrile interaction from pyrolyzed PAN/S to prevent lithium polysulfide shuttling [21]. Hwang et al. reported that sulfur composite with carbonized PAN (c-PAN/S) can also inhibit polysulfide dissolution, resulting in reversible electrochemical behavior over 300 cycles [19]. Recently, our group demonstrated a nitrogen-doped mesoporous carbon-sulfur composite with a high sulfur loading (4.2 mg-S/cm^2), in which the N-doped carbon promoted the formation of S–O bonds, which assisted the chemisorption sulfur and polysulfides as well as improved the distribution of the discharge products in the cathode [6,28].

Despite these achievements, designing facile synthetic route for sulfur-based cathode materials with a high conductivity, porosity, and favorable surface functionality, has been challenging. First, most chemisorption-capable carbons do not have high conductivity; for example, in the case of N-doped carbon, the number of functional groups decreases with increase of heat treatment temperature [30,31]. Second, most cathodes using functionalized sulfur/carbon composites (e.g., pyrolyzed polyacrylonitrile/sulfur (*p*PAN/S)) have failed to achieve good electrochemical performance with high sulfur content (>50%) due to low sulfur adsorption ability and high resistivity of the composite [20,24,25]. Nuli et al. reported that there was a trade-off between the sulfur content and electrochemical performance of pyrolyzed PAN/S (*p*PAN/S) composite since there was more elemental sulfur adsorbed on the surface of the composite at higher sulfur content, leading to poor cycling performance [20,24].

In this work, we demonstrate the preparation of a novel porous spherical nanocomposite of sulfur and pyrolyzed polyacrylonitrile-Ketjenblack carbon (*p*PAN-KB/S) via high throughput aerosol-assisted process and its application as cathode material for high sulfur loading Li–S batteries [14,32]. The advantage of our *p*PAN-KB/S composites (sulfur loading: *ca.* 72%) are based on the combination of high conductivity and physisorption abilities of KB and the strong chemical bonding abilities of *p*PAN; the internal sulfur was trapped inside the KB carbon by physical adsorption while the external sulfur was anchored to the framework of *p*PAN via chemical interaction. Taking advantage of these characteristics, the *p*PAN-KB/S composite exhibited a high capacity of 856 mAh/g (based on sulfur) after 100 cycles at 0.5C rate (1C: 1.68 A/g) and a good rate capability at a high current density (431 mAh/g at 5C). Moreover, a *p*PAN-KB/S electrode with high sulfur loading (*ca.* 4.4 mg-S/cm^2) exhibited superior electrochemical performance (cycle stability and rate capability) compared with *p*PAN/S and KB/S based cathodes with similar sulfur loading.

2. Experimental

2.1. Synthetic procedures

Porous spherical composite of polyacrylonitrile-Ketjenblack (PAN-KB): Porous spherical particles of PAN-KB were synthesized by an aerosol-assisted method using a mixture of polyacrylonitrile (PAN, average Mw. 150,000, Sigma–Aldrich) and Ketjenblack (EC-600JD, AkzoNobel) dispersed in dimethylformide (DMF) as the precursor. For the preparation of precursor, typically, 4 g of Ketjenblack (KB) carbon black and 1 g of PAN were mixed and dispersed in DMF at room temperature until the components were homogeneously distributed. To synthesize the porous spherical composite of PAN-KB, the above-described precursor was sent through an aerosol atomizer (model 3076, TSI Inc.) using nitrogen as a carrier gas [14,32]. The aerosolized precursor was passed through a ceramic tube heated to 300 °C. The porous composite particles of PAN-KB were then collected in a filter.

Porous composite of pyrolyzed PAN-KB and sulfur (pPAN-KB/S): The sulfur composite with pyrolyzed PAN-KB (*p*PAN-KB/S) was prepared by heating the mixture of PAN-KB composite and sulfur at 400 °C in argon atmosphere for 8 h. Considering the evaporation of the sulfur at this temperature, the initial sulfur content in the composites and resting time was controlled in order to obtain a composite with *ca.* 72% sulfur content. The sulfur content (*ca.* 72%) of the product was calculated after sulfur loading by elemental analysis using combustion elemental analyzer. Typically, 1.0 g of sublimed sulfur was mixed with 0.3 g of porous PAN-KB composite in an Ar filled vessel (20 mL). Then, the Ar filled vessel was heated to 400 °C at the rate of 2 °C/min, then kept 400 °C for 8 h. During the sulfur filling process, the molten sulfur filtrated into the pores or coated on the surface of the porous carbon, due in part to the high-surface-area-enabled adsorption of sulfur on porous carbon [2,4,14,24]. At the same time, PAN was pyrolyzed into a pyridine type polymer via a sulfur-induced dehydrogenation reaction [19,20]. Finally, the product was obtained after the composite was naturally cooled to room temperature. After sulfur embedding, the *p*PAN-KB/S composite was tested as an electrode material for lithium-sulfur batteries.

2.2. Characterizations

The size and morphology of the synthesized products were

obtained by transmission electron microscopy (TEM, JEOL-1200) at an accelerating voltage of 80 kV. High-resolution transmission electron microscopy (HR-TEM) images were taken on a field emission microscope JEOL-2010F at an accelerating voltage of 200 kV. Scanning electron microscopy (SEM) images were obtained with a NOVA NanoSEM 630 scanning electron microscope at an accelerating voltage of 1.5 kV. The nanocrystalline structure of the material was analyzed by X-ray diffraction (XRD) using a Rigaku Dmax-2000 X-ray powder diffractometer with CuKα radiation ($\lambda = 1.5418$ Å) under an operating voltage and current of 40 kV and 30 mA, respectively. The data were collected over a 2θ range between 15 and 60°. For the measurement of loaded sulfur, we measured the mass difference of the sample before and after sulfur loading. In addition, thermogravimetric analysis (TGA) was also carried out to analyze the sulfur content in the composite using a TA instruments SDT 2960, with a heating rate of 10 °C/min under nitrogen atmosphere. For the analysis of elemental composition of the sample, we used CHNS elemental analyzer (PerkinElmer 2400 series II CHNS/O system). The Raman spectra were obtained with a Renishaw Microscope Raman Spectrometer using a backscattering geometry. Spectra were averaged over 20 accumulations and the laser power was kept 2.5 mW. For the pore structure analysis, nitrogen sorption isotherms were carried out at 77 K with a Micromeritics ASAP 2020 analyzer (Micromeritics Instrument Corporation, Norcross, GA). Specific surface areas were calculated by the Brunauer–Emmett–Teller (BET) method using the adsorption branch in a relative pressure range from 0.04 to 0.25. The pore size distribution was calculated from adsorption branch of the N_2 isotherm with the Barrett–Joyner–Halenda (BJH) method. Before the porosity measurement, the sample was degassed at 150 °C for 6 h under vacuum to remove pre-adsorbed moiety on the surface of material. Electrical resistivity of powder materials was measured by compressing the powder in a cylindrical space and getting its resistance, which was then converted to conductivity and resistivity using the geometrical parameters of the cylindrical space. The pressure among powder particles was controlled with the force of compression.

2.3. Electrochemical measurements

The electrodes were prepared by infiltration of a solution of *p*PAN-KB/S composite dispersed in 1-methyl-2-pyrrolidinone (NMP, Aldrich) into carbon paper. The *p*PAN-KB/S composite-infiltrated carbon paper was dried at 50 °C under vacuum for 12 h. Finally, 1.13 cm^2 discs of carbon paper were cut from the coated carbon paper and used as the cathode. Sulfur loading of each cathode was varied approximately from *ca.* 1.7 mg/cm^2 for low sulfur loading to *ca.* 4.4 mg/cm^2 for high sulfur loading. Electrochemical tests of these electrode materials were performed using CR2016-type coin cells with the porous carbon-sulfur composite as the cathode and pure lithium metal foil (99.9%, Aldrich) as the counter electrode. The electrolyte was 1 M bis(trifluoromethane) sulfonimide lithium salt (LiTFSI, Sigma–Aldrich) and 0.1 M lithium nitrate ($LiNO_3$, Sigma–Aldrich) dissolved in a mixture of 1,3-dioxolane (DOL, Sigma–Aldrich) and dimethoxymethane (DME, Sigma–Aldrich) (DOL:DME, 1:1 v/v). Typically, we used 12 μL of electrolyte for low sulfur loading and 50 μL of electrolyte for high sulfur loading. There can be some difference (~1 μL) in the amount of electrolyte per each batch since some fraction of the electrolyte may have evaporated or spilled out during assembly. The ratio of sulfur to electrolyte is kept *ca.* 12 mL/g for both low and high sulfur loading. It should be noted that these are the amounts of electrolyte added into cells, rather than the precise amounts of electrolyte in the cells. A polypropylene membrane (Celgard 2400) was used as a separator film. The cells were assembled in an argon-filled glove box. The cells were cycled in the voltage range of 3.0 V–1.7 V using a BT-2043 Arbin battery testing system. All capacity values were calculated on the basis of sulfur mass. The cell was rested for 2 h before cycling. Cyclic voltammetry measurements were also carried out on coin cells at a scan rate of 0.1 mV/s between 1.5 V and 3.0 V *vs.* Li^+/Li using a CHI electrochemical station. The electrochemical impedance spectroscopy (EIS) was additionally performed over a frequency range of 1 MHz - 0.01 Hz using the Solartron electrochemical test station. All electrochemical measurements were performed at room temperature.

3. Results and discussion

The porous spherical *p*PAN-KB/S composite was prepared by an aerosol-assisted process [14,32] and subsequent embedding of sulfur at 400 °C [2,14]. Typically, ~2 g of PAN-KB composite were produced per batch. This could be scaled-up by connection of parallel aerosol apparatuses. Scheme 1 (and Scheme S1) illustrates the morphological (Scheme 1 top) and molecular (Scheme 1 bottom) change in the structure of the composite from the precursor to a thermally stable hetero-cyclic compound after the dehydrogenation and cyclization of PAN polymer by heat treatment and sulfur infiltration into PAN-KB at 400 °C [19–22,25]. A solution of PAN and KB (with a weight ratio of 1:4) in dimethylformamide (DMF) was used as the feeding precursor. An atomization process, using nitrogen as the carrier gas, continuously generated aerosol droplets (Scheme 1a). The aerosol precursor droplets passed through a heating zone (300 °C) and were converted into PAN-KB composite, where 30–40 nm sized Ketjenblack carbon (KB) was homogeneously mixed with the PAN polymer matrix to form an aggregated porous structure (Scheme 1b). The subsequent loading of sulfur into the PAN-KB under argon atmosphere at 400 °C enabled the formation of the robust composite *p*PAN-KB/S after thermal treatment. During sulfur loading at 400 °C, polymer chains of PAN were cyclized and dehydrogenated by losing hydrogen sulphide (H_2S) while the resulting PAN-derived carbon matrix was sulfurized by low order sulfur (S_x, x: 2–4) at high temperature from elemental sulfur (S_8) to form the *p*PAN-KB/S composite [19,20,25]. The final sulfur composites had a structure comprised of sulfur molecules embedded within the pyrolyzed PAN and KB matrix with a particle size between 300 nm and 1 μm. Specifically, in the sulfurized PAN (*p*PAN/S), nitrogen in PAN interacts with sulfur by chemical interaction while the KB in KB/S accommodates sulfur on its nanopores and provides facile electronic conduction pathways (Scheme 1c).

Fig. 1 shows electron microscope images of porous spherical PAN-KB (Fig. 1a–c) and *p*PAN-KB/S (Fig. 1d–g). Fig. 1a shows a scanning electron microscope (SEM) image of the polysized porous spherical PAN-KB composite, showing its size range of approximately 300 nm to 1 μm (centered at around 700 nm). Consistent with the SEM observation, the transmission electron microscope (TEM) image (Fig. 1b) shows that the average diameter of the PAN-KB is *ca.* 700 nm and KB particles are homogeneously distributed throughout the composite particle supported by PAN-derived carbon. The high resolution TEM image (Fig. 1c and f) shows that the KB has partly graphitized carbon (dashed circle and arrows), which should have high conductivity. The TEM images (Fig. 1b and c) also displays that PAN-KB has highly porous structure created not only by the inherent porous structure of KB (Fig. 1c) but also by the interparticle spaces generated among the particles. Fig. 1d–h and Fig. S1 show the TEM and SEM images and the elemental distribution (carbon, nitrogen, and sulfur) for *p*PAN-KB/S. Fig. 1d and e shows that the *p*PAN-KB/S composite maintains its spherical shape after pyrolysis during sulfur loading. The energy dispersive X-ray spectroscopy (EDS) elemental maps of *p*PAN-KB/S are shown in Fig. 1g and h. No large particles of sulfur are observed on the exterior of the

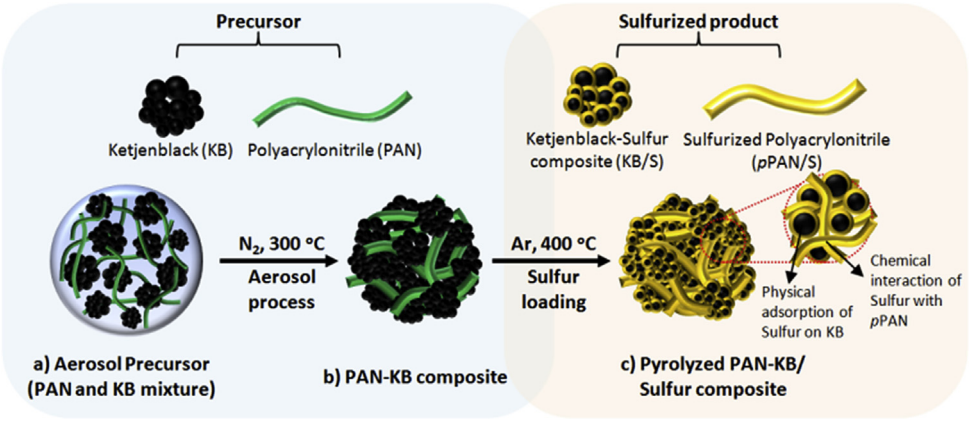

Scheme 1. Formation process and structural changes of porous spherical pPAN-KB/S composite during the carbonization and sulfurization. (a) Precursor (pristine PAN and KB before aerosol process); (b) aerosol product of porous spherical PAN-KB composite; (c) pyrolyzed PAN-KB/S (pPAN-KB/S) composite after sulfur loading at 400 °C under argon atmosphere.

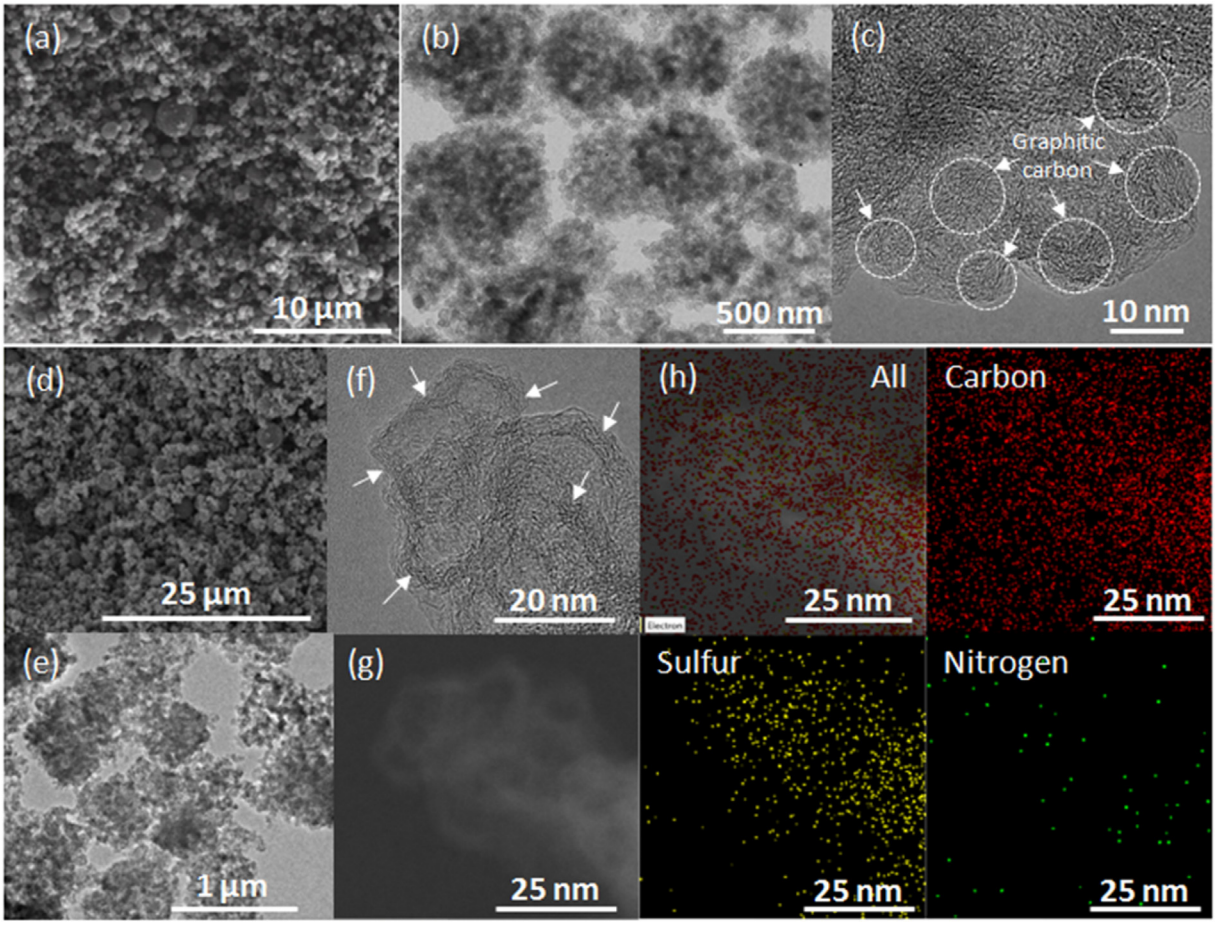

Fig. 1. Morphological analysis of (a–c) PAN-KB composite: (a) SEM image; (b) TEM and (c) high resolution TEM image. Morphological analysis of (d–h) *p*PAN-KB/S composite: (d) SEM image (e) TEM image, (f) high resolution TEM image. (g,h) TEM image for elemental analysis and (e) its elemental mapping (All, carbon (red), sulfur (yellow), nitrogen (green)). (For interpretation of the references to color in this figure legend, the reader is referred to the web version of this article.)

*p*PAN-KB/S composite particles (Fig. 1e and Fig. S1a), implying that sulfur is uniformly distributed in the carbon matrix of the *p*PAN-KB/S composite [14]. The homogeneous distribution of nitrogen (Fig. 1h and Fig. S1c) also suggests structural homogeneity of the *p*PAN-KB/S composite. We calculated the elemental composition of the *p*PAN-KB/S using CHNS elemental analyzer and carbon, nitrogen, and sulfur contents of composite are calculated as 27, 1, 72%, respectively. It is noteworthy that the sulfur amount is consistent with the result calculated by thermmogravimmetric analysis (Fig. S2) or by the measurement of sample mass difference before and after sulfur loading (Table S1).

Fig. 2 displays X-ray diffraction (XRD) patterns for the pristine

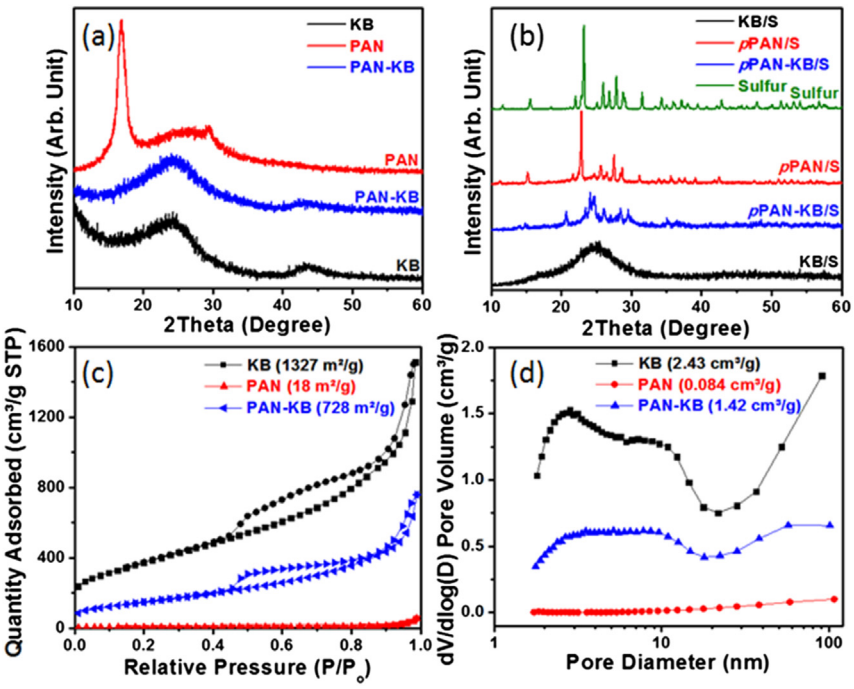

Fig. 2. Structural analysis of KB, PAN, and PAN-KB composite. X-ray diffraction of (a) pristine after sulfur loading (b); (c) N_2 adsorption–desorption isotherms (inset: BET surface area) and (d) pore size distribution (inset: pore volume).

PAN, PAN-KB, and KB (Fig. 2a), and their corresponding sulfur composites (sulfur content: *ca.* 72%) (Fig. 2b). The XRD patterns for pristine PAN exhibited a major peak at a 2θ of 17° corresponding to the (110) plane of the PAN crystal structure (Fig. 2a) [19,20]. The XRD patterns for *p*PAN/S exhibited crystallized sulfur peaks with a broad diffraction peak at 24°, but did not clearly show any new phases with C–S bond and the signature peak (17°) of pristine PAN (Fig. 2b), indicating the presence of large particles of sulfur in the *p*PAN/S composite [19,20]. The XRD patterns for KB (Fig. 2a) showed broad peaks at around 24° and 44°, which indicated an amorphous structure, while partly graphitized carbon was not clearly observed [4,14]. For the KB/S composite (Fig. 2b), the characteristic peaks of crystalline sulfur were not detectable, suggesting the small size of the embedded sulfur confined within the pores. The XRD pattern for the PAN-KB (Fig. 2a) was more similar to that of KB than to that of PAN since the composite consisted mostly of KB (PAN:KB = 1:4 wt.). For *p*PAN-KB/S composite (Fig. 2b and S3), crystalline orthorhombic sulfur peaks were not clearly observed due to dissociation of sulfur molecule (S_8) at high temperature (400 °C) [14]. Instead, new peaks corresponding to species formed by incorporation of sulfur into *p*PAN-KB/S were observed [14].

Fig. 2 also illustrates the N_2 sorption isotherms (Fig. 2c) and the pore size distributions (Fig. 2d) for PAN, KB, and the PAN-KB composite. The surface area for these samples varied from 18 m^2/g to 1327 m^2/g while the pore volume varied from 0.084 to 2.43 m^3/g; PAN had the lowest surface area and pore volume, while KB had the highest. Due to the large KB content in the PAN-KB composite, PAN-KB and KB exhibited a similar isotherm curve (type IV) with a condensation step within a narrow relative pressure range and type H1 hysteresis loops. These features are indicative of cylindrical mesopores (Fig. 2c) [14,33]. The PAN-KB composite also had a similar pore size distribution to that of KB, which confirmed the large porosity contribution of KB (Fig. 2d). The high porosity is expected to enable effective storage sulfur and polysulfides [2,4,5,14].

Raman spectroscopy was used to characterize the chemical structure and bonding of KB, PAN-KB, sulfur, and the sulfur composites, as shown in Fig. 3. KB and PAN-KB both have peaks at 1349 cm^{-1} and 1587 cm^{-1}, corresponding to breathing of sp^3 carbon bonds in the disordered carbon (the D band) and the stretching of sp^2 carbon bonds in the graphite planes (the G band), respectively. Sulfur exhibits peaks characteristic of its orthorhombic crystal structure at 220 cm^{-1} (S–S bending) and 479 cm^{-1} (S–S stretching) [34,35]. The KB/S composite has a very similar spectrum to that of KB, showing no evidence of peaks related to either S–S or C–S bonds. This indicates both that no new bonds between sulfur and KB were formed during sulfur loading, and that the sulfur was able to infiltrate into the pores of the KB framework. On the other

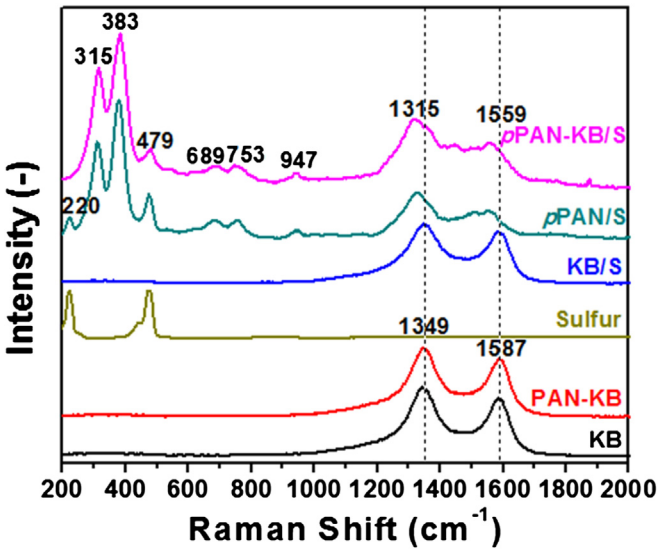

Fig. 3. Raman spectra for sulfur, PAN-KB, KB and their sulfur composites (*p*PAN/S, KB/S and *p*PAN-KB/S).

hand, *p*PAN/S exhibits peaks characteristic of elemental sulfur. The detected elemental sulfur is likely the free sulfur within the composite, the presence of which can be clearly seen from the XRD pattern of *p*PAN/S in Fig. 2b, as discussed above. Additional peaks also occur at 315, 383, 689, 759, and 947 cm^{-1}, corresponding to C–S bonds and suggesting that sulfur was chemically bonded with carbon from pyrolyzed PAN [22–25,34]. There is also a shift in the peaks representative of the D and G bands from KB and PAN-KB in the *p*PAN/S spectrum, possibly due to the formation of a cyclic PAN structure after pyrolysis [19,20,22–24,34]. The *p*PAN-KB/S had a very similar spectrum to that of the *p*PAN/S composite. The only peak not present in the *p*PAN-KB/S spectrum from the *p*PAN/S spectrum is the S–S bending mode. Despite small peak of S–S stretching at 479 cm^{-1} in the *p*PAN-KB/S spectrum, attenuated peak intensity may indicate only small amount of sulfur coated on the surface of *p*PAN-KB/S. This difference indicates that sulfur within the composite is either chemically incorporated in the *p*PAN or infiltrated into the KB pores, and is in good agreement with the lack of crystalline sulfur peaks in the XRD pattern of *p*PAN-KB/S in Fig. 2b [14,19,22,25,34,35].

Since electrode conductivity is a key factor in the capacity and rate performance of sulfur cathodes, the conductivities of *p*PAN/S, *p*PAN-KB/S, and KB/S electrodes with two different sulfur loadings in electrode (*ca.* 1.7 and 4.4 mg-sulfur/cm^2) were measured under various pressures, as shown in Fig. 4. The conductivities of each material before and after sulfur loading are shown in Fig. S4. At both low and high loadings, KB/S electrodes were found to have the highest conductivities. While *p*PAN-KB/S electrodes had lower conductivities than KB/S electrodes, they were still higher than those of *p*PAN-S electrodes. This is likely due to the poor carbonization of PAN at the low temperature and to its covalent bonding with sulfur in the *p*PAN/S [19,25]. The conductivity differences became even more pronounced at higher sulfur loading. Overall, the KB played an important role not only in enhancing the porosity but also in improving the conductivity of the composite.

Fig. 5 compares the electrochemical performance of KB/S, *p*PAN/S, and *p*PAN-KB/S. The cells were cycled at a current density of 0.5C (1C = 1680 mA/g) between 1.7 and 3.0 V (vs. Li/Li^+) after initial activation at 0.1C for the first two cycles. All specific capacities shown are based on the mass of sulfur in the composites. Fig. 5a shows typical charge–discharge voltage profiles at 0.5C for each composite. The voltage profile suggests that two different discharging phenomena occurred. Two discharge voltage plateaus around 2.3 V and 2.0 V correspond to the reduction of elemental sulfur to long chain lithium polysulfides (Li_2S_n, $6 \leq n < 8$) and to short chain lithium sulfide (Li_2S_2, Li_2S), respectively, characteristic of discharge profiles from porous carbon-sulfur composites [2,4,7,14]. At the same time, the covalently bonded sulfur chain is broken to form lithiated polysulfides. Some of these polysulfides remain covalently bonded to the polymer backbone while the rest of them dissociated into the electrolyte. As discharge proceeds, insoluble Li_2S is formed on the conducting carbon (KB) surface and the lithiated polysulfides in the *p*PAN/S gradually decreases. Further discharging results in the breakdown of the C–S bonds and the formation of carbon-conjugated bonds and production of lithium sulfide. Upon subsequent charging, the conjugated polymer backbone first loses electrons to form delocalized radical cations, which immediately trap Li_2S and form C–SLi seeds. Further charging results in the growth of the sulfur chain from the C–SLi seeds. In the entire discharging and charging process, soluble polysulfides are formed from KB/S while a redox reaction takes place between the solid PAN/S and the solid Li_2S [19,25].

It is noted that a high coulombic efficiency of >100% is observed at the first cycle (Fig. S5). We believe that an irreversible formation of short chain polysulfide (Li_2S_2) and side reaction related with the porous carbon may account for the large irreversible capacity in the first cycle [36]. In subsequent cycles, the coulombic efficiency became stabilized at >99%, which is attributed to the chemical interaction of the nitrile group in *p*PAN with polysulfides combined with the optimized pore structure of the composite [4,14,20–23].

The optimized porosity and composite structure was assessed by changing the ratio of PAN and KB. As demonstrated in Fig. S6 tested at 0.1C which is the same as for Fig. 5, the performance of aerosol-generated *p*PAN-KB/S is further tunable by regulating the amount of PAN and KB mainly due to the difference in the porosity of various *p*PAN-KB/S composites (Fig. S7), which is in line with previous reports [4,14]. In addition, enhanced performance of *p*PAN-KB (1:4)/S compared with *p*PAN-KB (1:1)/S may suggest that highly conductive and porous KB more contributes to improve the performance of *p*PAN-KB/S rather than *p*PAN does. Nevertheless, both *p*PAN and KB are important to attain high capacity and long cycle stability of the *p*PAN-KB/S composite due to their different role in the physisorptions and chemisorptions. On the other hand, the aerosol-generated composite performed better than a simply-mixed *p*PAN-KB/S sample (Fig. S8) and previously reported composite of PAN/carbon and sulfur [25]. The simply-mixed *p*PAN-KB/S was prepared by simply mixing PAN and KB followed by sulfur loading at 400 °C under Ar atmosphere. Both simply-mixed and aerosol *p*PAN-KB/S were compared at the same test condition and sulfur loading (70%). The superior performance of the aerosol-generated *p*PAN-KB/S is attributed to higher conductivity, more uniform sulfur distribution, and the spherical morphology of the particles themselves, which enable better electrode packing [14,21–23,28].

Fig. 5c shows the rate performance of the sulfur composites at current densities between 0.1C and 5C. Cells with *p*PAN-KB/S

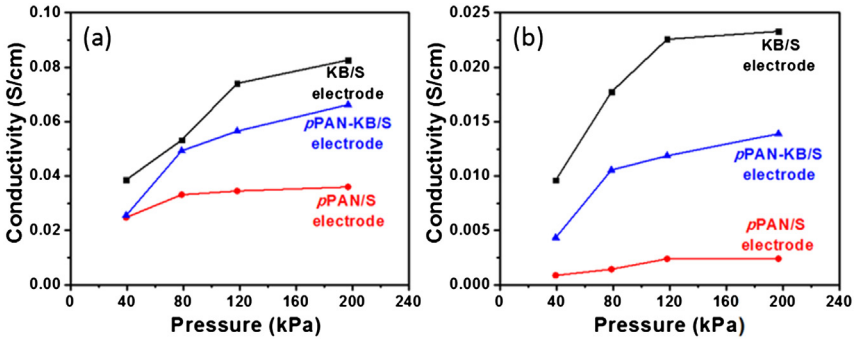

Fig. 4. Electrical conductivities of electrodes of *p*PAN/S, *p*PAN-KB/S and KB/S (a) at low sulfur loading (*ca.* 1.7 mg-S/cm^2) and (b) at high sulfur loading (*ca.* 4.4 mg-S/cm^2) measured at various pressures.

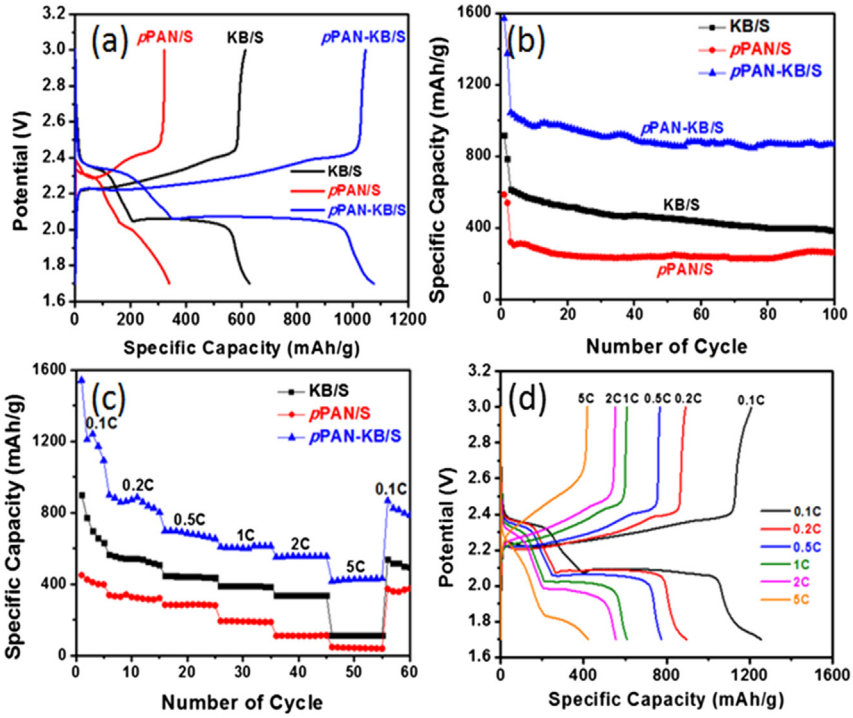

Fig. 5. Electrochemical performance. (a) Comparative voltage profile at 0.5C (0.84 A/g), (b) Cycling performance (0.5C) for the reversible charge capacity of the sample measured at 0.1C (0.168 A/g) for the first two cycles for initial activation and at 0.5C for the rest of the cycles (3–100), (c) Rate capability at various C-rates (0.1C–5C), (d) Voltage profile of *p*PAN-KB/S measured at various C-rates (0.1C–5C). (Sulfur loading: *ca.* 1.7 mg-sulfur/cm^2).

cathodes showed superior rate performance at every current rate. While the covalent bonds can decrease polysulfide dissolution in *p*PAN/S, *p*PAN/S still suffers from a low electrical conductivity (Fig. 4), which explains the poor rate performance. In addition, the presence of large particles of crystalline sulfur on *p*PAN/S, as observed by XRD (Fig. 2) and Raman spectra (Fig. 3), would decrease the overall conductivity and additionally would be harder to be exploited electrochemically, making the rate performance of *p*PAN/S worse [2,4,14]. Cells made with KB/S showed better performance compared to *p*PAN/S, having a higher conductivity, surface area, and pore volume. KB/S, however, suffered from significant polysulfide dissolution. The performance of KB/S electrodes in our result shows inferior performance to that of previous reports [11,12]. We believe the difference of the performance can be attributed to the different electrochemical test condition such as amount of electrolyte per electrode or ratio of electrolyte to sulfur [6,11]. The *p*PAN-KB/S composite combined the C–S covalent bonds of *p*PAN/S with the high conductivity, surface area, and pore volume of KB/S, which contributed to its superior rate performance [24,37]. Fig. 5d displays the voltage profile of the *p*PAN-KB/S cells at different current densities. The voltage profiles do not show significant polarization until 2C rate is applied, indicating efficient Li-ion transport and electron transport during the charge/discharge process [14]. Furthermore, the *p*PAN-KB/S cells showed stable performance after prolonged testing at 5C (Fig. S9), with high capacity of 391 mAh/g and coulombic efficiency of 99% after 400 cycles.

The improved electrochemical performance of the *p*PAN-KB/S composite is attributed to its unique composite structure. *p*PAN/S provides strong C–S covalent bonds to reduce the amount of sulfur and polysulfides dissolved in the electrolyte, while KB/S provides a high electronic conductivity, surface area, and pore volume to accommodate a high sulfur content. These benefits were combined in the *p*PAN-KB/S composites, leading to improved capacity and cycling stability.

For practical applications, sulfur cathodes with high sulfur content and high areal sulfur loading are required [6]. However, many high sulfur content and loading cathodes prepared to-date have been shown to suffer from severe polarization, poor cycling stability, low capacity, and low coulombic efficiency [4,5,14]. The cycling performance of *p*PAN/S, *p*PAN-KB/S, and KB/S with high sulfur loading (*ca.* 4.4 mg-S/cm^2) was therefore studied, as shown in Fig. 6. The gravimetric and volumetric specific capacities of *p*PAN-KB/S were shown to be quite high (513 mAh/g and 576 mAh/cm^3 at 0.5C after 100 cycles, respectively) when cycled at a low C-rate of 0.1C (0.168 A/g) for the first two cycles and 0.5C (0.84 A/g) for the subsequent cycles, with a coulombic efficiency >99% when switched to 0.5C (Fig. S10). The tap densities of *p*PAN/S, KB/S, and *p*PAN-KB/S were measured to be 0.521, 0.472 and 1.13 g/cm^3, respectively. The high tap density of *p*PAN-KB/S contributed to its higher volumetric capacity [12,14]. It is noteworthy that, compared with conventional nitrogen rich carbon-sulfur composite (e.g., *c*-PAN/S and nitrogen-doped carbon/S) with high sulfur loading (>4 mg-S/cm^2), our result in this work shows superior performance to that of N-rich carbon/S composites in the high-rate cycle test owing to enhanced sulfur adsorption ability (*p*PAN) and low resistivity (KB) of the composite [6,23,28,29]. The good electrochemical performance of *p*PAN-KB/S at high sulfur loading suggests that the combined effects of conductivity and porosity of the KB and chemical functionality of *p*PAN/S are of the utmost importance and that this cathode has a potential to be applied to practical battery applications, such as electric vehicles.

4. Conclusions

In summary, we prepared a porous spherical pyrolyzed polyacrylonitrile-Ketjenblack/sulfur (*p*PAN-KB/S) composite with high sulfur loading (ca. 72%) through an aerosol-assisted process for

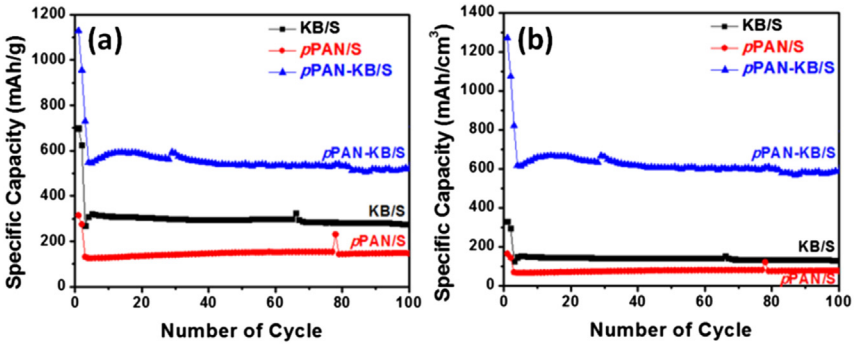

Fig. 6. Comparative cycle stability of (a) *p*PAN/S, KB/S and *p*PAN-KB/S with high sulfur loading at 0.5C (0.84 A/g); (b) Volumetric capacity of *p*PAN/S, KB/S and *p*PAN-KB/S (Sulfur loading: *ca*. 4.4 mg-S/cm^2).

application in lithium-sulfur batteries. This cathode material showed good electrochemical performance (capacity retention of 866 mAh/g after 100 cycles at 0.5C), which is attributed to 1) the uniform distribution of sulfur embedded in the porous and conductive PAN-KB, 2) the strong chemical interactions between sulfur and polysulfides with *p*PAN, and 3) the enhancement of the conductivity and structural stability with KB. The cell polarization was also suppressed, illustrated by the good cycling and rate performances. Particularly, the *p*PAN-KB/S electrode with high sulfur loading (4.4 mg-S/cm^2) exhibited impressive gravimetric and volumetric capacities (513 mAh/g and 576 mAh/cm^3, respectively, based on sulfur) after 100 cycles at a 0.5C rate and coulombic efficiencies of >99% after the activation. These unique properties of the porous spherical *p*PAN-KB/sulfur composite, along with the simple, robust, and scalable fabrication process, which make this composite attractive for further investigation for Li–S battery applications.

Acknowledgments

This work was supported by the Assistant Secretary for Energy Efficiency, Renewable Energy, Office of Vehicle Technologies of the U.S. Department of Energy under Contract No. DE-EE0005475 (D. Wang) and by the Energy Efficiency and Resources Program of the Korea Institute of Energy Technology Evaluation and Planning (KETEP) grant funded by the Korea government Ministry of Trade, Industry and Energy (No. 20112010100150) (Y. Jung).

Appendix A. Supplementary data

Supplementary data related to this article can be found at http://dx.doi.org/10.1016/j.jpowsour.2015.10.013.

References

[1] P. Bruce, S. Freunberger, Nat. Mater 11 (2012) 19–29; Z. Wang,, L. Zhou, X. W. Lou, Adv. Mater. 24(2012) 1903–1911; X. Lai, J. E. Halpert, D. Wang, Energy Environ. Sci. 5 (2012) 5604–5618.
[2] A. Manthiram, Y. Fu, Y.-S. Su, Acc. Chem. Res. 46 (2012) 1125–1134. X. Ji, K. T. Lee, L. F. Nazar, Nat. Mater. 8(2009) 500–506.
[3] Y.V. Mikhaylik, J.R. Akridge, J. Electrochem. Soc. 151 (2004) A1969–A1976.
[4] X. Li, Y. Cao, W. Qi, L.V. Saraf, J. Xiao, Z. Nie, J. Mietek, J.-G. Zhang, B. Schwenzer, J. Liu, J. Mater. Chem. 21 (2011) 16603–16610.
[5] X. Liang, Z. Wen, Y. Liu, H. Zhang, L. Huang, J. Jin, J. Power Sources 196 (2011) 3655–3658.
[6] J. Song, T. Xu, M.L. Gordin, P. Zhu, D. Lv, Y.-B. Jiang, Y. Chen, Y. Duan, D. Wang, Adv. Funct. Mater. 24 (2013) 1243–1250. J. Song, M. L. Gordin, T. Xu, S. Chen, Z. Yu, H. Sohn, J. Lu, Y. Ren, Y. Duan, D. Wang, Angew. Chem. Inter. Ed. 54(2015) 4325–4329; L. Zhou, X. Lin, T. Huang, A. Yu, J. Mater. Chem. A 2 (2014) 5117-5123; J. Zhang, Z. Dong, X. Wang, X. Zhao, J. Tu, Q. Su, G. Du, J. Power Sources 270 (2014) 1-8; A. Schneider, C. Weidmann, C. Suchomski, H. Sommer, J. Janek, T. Brezesinski, Chem. Mater. 27 (2015), 1674-1683.
[7] Y.S. Su, A. Manthiram, Chem. Commun. 48 (2012) 8817–8819. S.-C. Han, M.-S. Song, H. Lee, H.-S. Kim, H.-J. Ahn, J.-Y. Lee, J. Electrochem. Soc. 150(2003) A889–A893; J. Guo, Y. Xu, C. Wang, Nano Lett. 11 (2011) 4288-4294; L. Yuan, H. Yuan, X. Qiu, L. Chen, W. Zhu, J. Power Sources 189 (2009) 1141-1146; S. Dörfler, M. Hagen, H. Althues, J. Tübke, S. Kaskel, M. J. Hoffmann, Chem. Commun. 48 (2012) 4097-4099; W. Ahn, K.-B. Kim, K.-N. Jung, K.-H. Shin, C.-S. Jin, J. Power Sources 202 (2012) 394–399.
[8] R. Elazari, G. Salitra, A. Garsuch, A. Panchenko, D. Aurbach, Adv. Mater 23 (2011) 5641–5644.
[9] H. Wang, Y. Yang, Y. Liang, J.T. Robinson, Y. Li, A. Jackson, Y. Cui, H. Dai, Nano Lett. 11 (2011) 2644–2647. Y. Qiu, W. Li, W. Zhao, G. Li, Y. Hou, M. Liu, L. Zhou, F. Ye, H. Li, Z. Wei, S. Yang, W. Duan, Y. Ye, J. Guo, Y. Zhang, Nano Lett. 14(2014) 4821–4827; M.-Q. Zhao, X.-F. Liu, Q. Zhang, G.-L. Tian, J.-Q. Huang, W. Zhu, F. Wei, ACS Nano 6 (2012) 10759-10769; B. Ding, C. Yuan, L. Shen, G. Xu, P. Nie, X. Zhang, Chemistry - A Eur. J. 19 (2013) 1013-1019; C. Xu, B. Xu, Y. Gu, Z. Xiong, J. Sun, X. S. Zhao, Energy Environ. Sci. 6 (2013) 1388-1414; J.-Z. Wang, L. Lu, M. Choucair, J. A. Stride, X. Xu, H.-K. Liu, J. Power Sources 196 (2011) 7030–7034.
[10] Y.S. Su, A. Manthiram, Nat. Commun. 3 (2012) 1166–1171. J. Song, Z. Yu, T. Xu, S. Chen, H. Sohn, M. Regula, D. Wang, J. Mater. Chem. A 2(2014) 8623–8627.
[11] B.O. Jeong, S.W. Kwon, T.J. Kim, E.H. Lee, S.H. Jeong, Y. Jung, Nanosci. Nanotechnol. 13 (2013) 7870–7874; C. Liang, N. J. Dudney, J. Y. Howe, Chem. Mater. 21(2009) 4724–4730; D.-W. Wang, G. Zhou, F. Li, K.-H. Wu, G. Q. Lu, H.-M. Cheng, I. R. Gentle, Phys. Chem. Chem. Phys. 14 (2012) 8703-8710; C. Villevieille, P. Novak, J. Mater. Chem. A 1 (2013) 13089-13092; S. Moon, Y. H. Jung, W. K. Jung, D. S. Jung, J. W. Choi, D. K. Kim, Adv. Mater. 25 (2013) 6547–6553; A. Jozwiuk, H. Sommer, J. Janek, T. Brezesinski, J. Power Sources 296 (2015) 454–461.
[12] P. Strubel, S. Thieme, T. Biemelt, A. Helmer, M. Oschatz, J. Brückner, H. Althues, S. Kaskel, Adv. Funct. Mater. 25 (2015) 287–297. J. Schuster, G. He, B. Mandlmeier, T. Yim, K. T. Lee, T. Bein, L. F. Nazar, Angew. Chem. Int. Ed. 51(2012) 3591–3595; T. Xu, J. Song, M. L. Gordin, H. Sohn, Z. Yu, S. Chen, D. Wang, ACS Appl. Mater. Interfaces 5 (2013) 11355–11362.
[13] B. Zhang, X. Qin, G.R. Li, X.P. Gao, Energy Environ. Sci. 3 (2010) 1531–1537.
[14] H. Sohn, M.L. Gordin, T. Xu, S. Chen, D. Lv, J. Song, A. Manivannan, D. Wang, ACS Appl. Mater. Interfaces 6 (2014) 7596–7606.
[15] Y. Fu, A. Manthiram, RSC Adv. 2 (2012) 5927–5929. Y. Yang, G. Yu, J. Cha, H. Wu, M. Vosgueritchian, Y. Yao, Z. Bao, Y. Cui, ACS Nano 5(2011) 9187–9193; J. Wang, J. Chen, K. Konstantinov, L. Zhao, S. H. Ng, G. X. Wang, Z. P. Guo, H. K. Liu, Electrochim. Acta 51 (2006) 4634–4638.
[16] H. Teoh, P.D. Metz, W.G. Wilhelm, Mol. Cryst. Liq. Cryst. 83 (1982) 297–306.
[17] L. Yin, J. Wang, J. Yang, Y.J. Nuli, Mater. Chem. 21 (2011) 6807–6810.
[18] Y. Zhang, Y. Zhao, Z. Bakenov, M.-R. Baba, A. Konarov, C. Ding, P. Chen, J. Electrochem. Soc. 160 (2013) A1194–A1198.
[19] T.H. Hwang, D.S. Jung, J.-S. Kim, B.G. Kim, J.W. Choi, Nano Lett. 13 (2013) 4532–4538.
[20] J.L. Wang, J. Yang, J.Y. Xie, N.X. Xu, Adv. Mater. 14 (2002) 963–965. J. Wang, J. Wang, C. Wan, K. Du, J. Xie, N. Xu, Adv. Funct. Mater. 13(2003) 487–492.
[21] J. Guo, Z. Yang, Y. Yu, H.D. Abruña, L.A. Archer, J. Am. Chem. Soc. 135 (2013) 763–767.
[22] X.-G. Yu, J.-Y. Xie, J. Yang, H.-J. Huang, K. Wang, Z.-S. Wen, J. Electroanal Chem. 573 (2004) 121–128. X. He, J. Li, M. Chen, J. Gao, C. Jiang, Electrochimica Acta 72(2012) 114–119.
[23] A. Konarov, D. Gosselink, T.N.L. Doan, Y. Zhang, Y. Zhao, P. Chen, J. Power Sources 259 (2014) 183–187. J. Fanous, M. Wegner, J. Grimminger, M. Rolff, M. B. M. Spera, M. Tenzer, M. R. Buchmeiser, J. Mater. Chem. 22(2012) 23240–23245; J. Fanous, M. Wegner, J. Grimminger, Á. Andresen, M. R. Buchmeiser, Chem. Mater. 23 (2011) 5024-5028; J. Fanous, M. Wegner, M. B. M. Spera, M. R. Buchmeiser, J. Electrochem. Soc. 160 (2013) A1169–A1170.
[24] L.C. Yin, J.L. Wang, F.J. Lin, J. Yang, Y. Nuli, Energy Environ. Sci. 5 (2012) 6966–6972.
[25] S.S. Zhang, Front. Energy Res. 1 (2013) 1–9. S. S. Zhang, Energies 7(2014) 4588–4601; T. Hara, A. Konarov, A. Mentbayeva, I. Kurmanbayeva, Z. Bakenov,

Front. Energy Res. 3, 22 (2015) 1–6.
[26] S. Evers, T. Yim, L.F. Nazar, J. Phys. Chem. C 116 (2012) 19653–19658. K. T. Lee, R. Black, T. Yim, X. Ji, L. F. Nazar, Adv. Energy Mater. 2(2012) 1490–1496; H. Kim, J. T. Lee, D.-C. Lee, A. Magasinski, W. Cho, G. Yushin, Adv. Energy Mater. 3 (2013) 1308-1315; H. Yao, G. Zheng, P.-C. Hsu, D. Kong, J. J. Cha, W. Li, Z. W. Seh, M. T. McDowell, K. Yan, Z. Liang, V. K. Narasimhan, Y. Cui, Nat. Commun. 5 (2014) 3943–3951.
[27] L. Ji, M. Rao, H. Zheng, L. Zhang, O.Y. Li, W. Duan, J. Guo, E.J. Cairns, Y. Zhang, J. Am. Chem. Soc. 133 (2011) 18522–18525. N. Li, M. Zheng, H. Lu, Z. Hu, C. Shen, X. Chang, G. Ji, J. Cao, Y. Shi, Chem. Commun. 48(2012) 4106–4108; F. Zhang, X. Zhang, Y. Dong, L. Wang, J. Mater. Chem. 22 (2012) 11452; W. Zhou, H. Chen, Y. Yu, D. Wang, Z. Cui, F. J. DiSalvo, H. D. Abruña, ACS Nano 7 (2013) 8801-8808; Z. Wang, Y. Dong, H. Li, Z. Zhao, H. Bin Wu, C. Hao, S. Liu, J. Qiu, X. W. D. Lou, Nat. Commun. 5 (2014) 5002-5009; W. Bao, Z. Zhang, W. Chen, C. Zhou, Y. Lai, J. Li, Electrochim. Acta 127 (2014) 342–348.
[28] X. Li, X. Sun, Front. Energy Res. 2 (2014) 1–9. X. Li, X. Li, M. N. Banis, B. Wang, A. Lushington, X. Cui, R. Li, T.-K. Sham, X. Sun, J. Mater. Chem. A 2(2014) 12866–12872.
[29] X.-G. Sun, X. Wang, R.T. Mayes, S. Dai, ChemSusChem 10 (2012) 2079–2085. F. Sun, J. Wang, H. Chen, W. Li, W. Qiao, D. Long, L. Ling, ACS Appl. Mater. Interfaces 5 (2013) 5630-5638; Z. Wang, X. Niu, J. Xiao, C. Wang, J. Liu, F. Gao, RSC Adv. 3(2013) 16775–16780.
[30] D.-S. Yang, S. Chaudhari, K.P. Rajesh, J.-S. Yu, ChemCatChem 6 (2014) 1236–1244. S. Shrestha, S. Asheghi, J. Timbro, W. E. Mustain, Appl. Catal. A: General 464 (2013) 233-242; Z. R. Ismagilov, A. E. Shalagina, O. Y. Podyacheva, A. V. Ischenko, L. S. Kibis, A. I. Boronin, Y. A. Chesalov, D. I. Kochubey, A. I. Romanenko, O. B. Anikeeva, T. I. Buryakov, E. N. Tkachev, Carbon 47(2009) 1922–1929.
[31] Y. Mao, H. Duan, B. Xu, L. Zhang, Y. Hu, C. Zhao, Z. Wang, L. Chen, Y. Yang, Energy Environ. Sci. 5 (2012) 7950–7955. K. K. R. Datta, V. V. Balasubramanian, K. Ariga, T. Mori, A. Vinu, Chem. Eur. J. 17, 3390-3397(2011); K. Fujisawa, T. Tojo, H. Muramatsu, A. L. Elias, S. M. Vega-Diaz, F. Tristan-Lopez, J. H. Kim, T. Hayashi, Y. A. Kim, M. Endo, M. Terrones, Nanoscale 3 (2011) 4359–4364.
[32] Q. Xiao, H. Sohn, Z. Chen, D. Toso, M. Mechlenburg, Z.H. Zhou, E. Poirier, A. Dailly, H. Wang, Z. Wu, M. Cai, Y. Lu, Angew. Chem. Int. Ed. 51 (2012) 10546–10551. H. Sohn, Z. Chen, Y. S. Jung, Q. Xiao, M. Cai, H. Wang, Y. Lu, J. Mater. Chem. A 1(2013) 4539–4545.
[33] K.S.W. Sing, D.H. Everett, R.A.W. Haul, L. Moscou, R.A. Pierotti, J. Rouquerol, T. Siemieniewska, Pure Appl. Chem. 57 (1985) 603–619.
[34] X. Yu, J. Xie, Y. Li, H. Huang, C. Lai, K. Wang, J. Power Sources 146 (2005) 335–339.
[35] X.G. Yu, J.Y. Xie, J. Yang, H.J. Huang, K. Wang, Z.S. Wen, J. Electroanal. Chem. 573 (2004) 121–128.
[36] R. Demir-Cakan, M. Morcrette, Gangulibabu, A. Gueguen, R. Dedryvere, J.M. Tarascon, Energy Environ. Sci. 6 (2013) 176–182.
[37] W. Wei, J. Wang, L. Zhou, J. Yang, B. Schumann, Y. Nuli, Electrochem. Commun. 13 (2011) 399–402.